Kinetic modelling of ELM-induced tungsten transport in a tokamak plasma

D.C. van Vugt,[1,2,a)] G.T.A. Huijsmans,[1,3] M. Hoelzl,[4] A. Loarte,[2] ASDEX Upgrade Team,[b)] and EUROfusion MST1 Team[c)]

[1)] *Eindhoven University of Technology, 5600MB Eindhoven, The Netherlands*

[2)] *ITER Organization, 13067 St. Paul Lez Durance Cedex, France*

[3)] *CEA Cadarache, IRFM, 13108 St. Paul Lez Durance Cedex, France*

[4)] *Max Planck Institute for Plasma Physics, Boltzmannstr. 2, 85748 Garching bei München, Germany*

(Dated: 26 March 2019)

Impurity accumulation in the core plasma leads to fuel dilution and higher radiative losses that can lead to loss of H-mode and to thermal collapse of the plasma and eventually even to a disruption in tokamaks. In present experiments, it has been shown that ELMs at sufficiently high frequency are required to prevent W accumulation in the core, by expelling impurities from the edge plasma region, thus preventing their penetration into the plasma core. We present a full-orbit particle extension of the MHD code JOREK suitable for simulating impurity transport during ELMs. This model has been applied to the simulation of an ELM crash in ASDEX Upgrade, where we have quantified the displacement of W particles across flux surfaces. The transport mechanism is shown to be the particle $E \times B$-drifts due to the electric field created by the MHD instability underlying the ELM. In- and outwards transport is observed as a series of interchange motions leading to a superdiffusive behaviour. This causes particles near the plasma pedestal to move outwards, but also particles outside of the pedestal to move inwards. This has important consequences for operation with W in ITER, where it is expected to be screened in the pedestal, and ELMs are shown here to increase the core W density. A comparison with existing diffusive modelling is made, showing a qualitative agreement and the limitations of this simplified modelling approach.

[a)]Electronic mail: d.c.v.vugt@tue.nl

[b)]See appendix of A. Kallenbach for the ASDEX Upgrade Team and the EUROfusion MST1 Team 2017 Nucl. Fusion 57 102015.

[c)]See author list of H. Meyer et al 2017 Nucl. Fusion 57 102014.

I. INTRODUCTION

Tokamak operation with tungsten (W) plasma facing components (PFCs) has many operational advantages regarding fuel retention and lower wall erosion, leading to increased lifetime of the PFCs. The PFC of the ITER divertor will be tungsten[1]. The main drawbacks for its application in fusion reactors concern W contamination of the core plasma and melting of the PFCs by transient events; although the melting temperature for W is the highest of any metal the energy fluxes in these events in a fusion reactor are expected to be large enough to potentially cause W PFC surface melting[2]. Sputtered W accumulating in the core plasma leads to higher radiative losses that can cause a back-transition from H- to L-mode, a thermal collapse of the plasma or even a disruption. Relative W concentrations in the range of a few 10^{-5} are expected to significantly decrease fusion performance in ITER and next step devices[3]. This pollution must be controlled to have reliable H-mode operation, for instance by triggering frequent ELMs with pellet injection or by vertical position oscillations. ELMs at sufficiently high frequency can prevent W accumulation in the core[4], by expelling impurities from the edge plasma region[5,6]. This effect is more pronounced for high-Z impurities given the large inwards edge neoclassical pinch that they are subject to and the ensuing edge impurity density peaking in present experiments. The effect of ELMs on high-Z impurity outflux in ITER, however, remains uncertain given the expected impurity screening in the plasma pedestal[7]. There is circumstantial evidence that in some cases ELMs can contribute to the increase of W influx in the core plasma that leads to an increase of edge radiation and a decrease of the pedestal temperature[8].

Besides preventing accumulation in the core, ELMs also play a role in creating impurities. The higher heat fluxes and plasma temperatures in the divertor region during an ELM greatly increase the sputtering yields and cause most of the impurity production[9]. It is thus important to keep the power fluxes impinging onto

the divertor during ELMs at a sufficiently low level that avoids melting of the W PFCs and large W impurity production. Calculating this impurity production and subsequent neoclassical transport in JOREK is currently under investigation but out of the scope of this article.

Heavy impurities can be transported up the fieldlines and neoclassically inwards by the temperature gradient force, until a balance with temperature screening effects is established. During the inter-ELM period this sets up a density profile, often with a peak in the pedestal top region, which is then altered strongly by the ELM[7,10].

The MHD instability causing the ELM creates strong electric fields, leading to perpendicular $E \times B$ flows with an RMS velocity of hundreds of m/s in the peeling-ballooning mode vortices in the outer regions of the plasma. This is much faster than either neoclassical or turbulent transport. Here, the transport of W due to the ELM MHD instability is evaluated by tracing the full orbits of collisionless Tungsten ions in the 3D perturbed electric and magnetic fields obtained from a JOREK[11,12] nonlinear MHD simulation of an ELM in ASDEX Upgrade[13].

This will provide insight into the nature of radial heavy impurity motion due to ELMs, which is important for present experiments and the extrapolation to ITER. In ITER, while unmitigated type-I ELMs are unacceptable in the 15MA plasma current experiments they are potentially acceptable at the half-current scenarios (up to 7.5 MA)[2]. Mitigated small ELMs, such as those triggered by pellet injection or by vertical kicks[14] are characterised by the same underlying MHD mode (i.e. ballooning-peeling mode), leading to an interchange motion of the tungsten distribution similar to that shown in the rest of this paper.

In this paper, we provide insight into the nature of this motion and the underlying physical mechanisms. Relevant questions are for instance whether the motion is caused by electric or magnetic field fluctations, and to what extent it can be described by a convection-diffusion model.

In Section II we introduce the kinetic particle extension to JOREK and explain the numerical methods used. Section III contains results for particle transport in a realistic multi-mode ($n = 1..8$) simulation of a type-I ELM in ASDEX Upgrade. We will discuss the validity of 1D diffusive ELM flushing modelling in Section IV. In Section V we summarize our findings and indicate directions for future research.

II. FULL-ORBIT PARTICLE TRACKING IN NONLINEAR MHD SIMULATIONS

To simulate W motion in time-varying fields, we have implemented a kinetic particle tracer and coupled it to the non-linear MHD code JOREK[11,12]. This section describes the algorithms used and provides an overview of the implementation. A diagram of the code operation is shown in figure 1. A more detailed description of this particle extension, including a feedback from the impurity distributions and the associated losses to the plasma (radiation, ionization, etc.) into the reduced MHD equations can be found in[15].

The charged particle trajectories are determined by the Lorentz force $\mathbf{F} = q\left(\mathbf{E} + \mathbf{v} \times \mathbf{B}\right)$, leading to orbits around the magnetic field lines. These are integrated with the well-known Boris integrator[16], a leap-frog type scheme[17]. The positions and velocities are staggered in time, shifted by $\Delta t/2$. The velocities are known at the half-timesteps, $\mathbf{v}^{n+1/2}$ and the positions are known at the full timesteps $\mathbf{x}^n$. The equation is written in centered difference form, where the magnetic term is centered by averaging $\mathbf{v}^{n-1/2}$ and $\mathbf{v}^{n+1/2}$, following[18]. The electric and magnetic fields are interpolated from the JOREK simulation at the particle location at the full timesteps $\mathbf{x}^n$.

$$\frac{\mathbf{v}^{n+1/2} - \mathbf{v}^{n-1/2}}{\Delta t} = \frac{q}{m}\left[\mathbf{E} + \frac{\mathbf{v}^{n+1/2} + \mathbf{v}^{n-1/2}}{2} \times \mathbf{B}\right], \tag{1}$$

If we substitute $\mathbf{v}^{n+1/2} = \mathbf{v}^{+} + \frac{q\mathbf{E}}{m}\frac{\Delta t}{2}$ and $\mathbf{v}^{n-1/2} = \mathbf{v}^{-} - \frac{q\mathbf{E}}{m}\frac{\Delta t}{2}$ into (1), $\mathbf{E}$ cancels

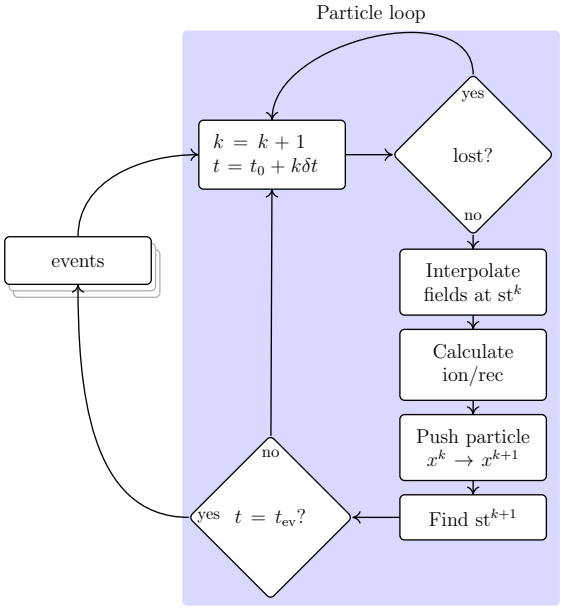

FIG. 1. Schematical view of the operations in the JOREK particle tracer. Events are used for diagnostic output, as well as for reading new JOREK output files.

entirely and we are left with

$$\frac{\mathbf{v}^+ - \mathbf{v}^-}{\Delta t} = \frac{q}{2m}\left(\mathbf{v}^+ + \mathbf{v}^-\right) \times \mathbf{B} \tag{2}$$

which produces a pure rotation of the velocity vector due to the magnetic field, leading to the energy-conservation properties of the Boris method. Extra accuracy is obtained here by replacing $f = \frac{q\Delta t}{2m}$ with $f' = \tan(f|\mathbf{B}|)/|\mathbf{B}|$ to reproduce the gyrofrequency exactly. In the JOREK cylindrical coordinate system (R, Z, ϕ)[12] the position update is determined as[19]

$$R^{n+1} = \sqrt{\left(R^n + v_R^{n+1/2}\Delta t\right)^2 + \left(v_\phi^{n+1/2}\Delta t\right)^2} \tag{3}$$

$$Z^{n+1} = Z^n + v_Z^{n+1/2}\Delta t \tag{4}$$

$$\phi^{n+1} = \phi^n + \sin^{-1}\left(\frac{v_\phi^{n+1/2}\Delta t}{R^{n+1}}\right). \tag{5}$$

Finally the velocity vector $v^{n+1/2}$ is rotated to match the change in ϕ

$$v_r^{n+1/2} \rightarrow \cos\alpha\ v_R^{n+1/2} + \sin\alpha\ v_\phi^{n+1/2} \tag{6}$$

$$v_\phi^{n+1/2} \rightarrow -\sin\alpha\ v_R^{n+1/2} + \cos\alpha\ v_\phi^{n+1/2} \tag{7}$$

$$\tag{8}$$

where $\alpha = \phi^{n+1} - \phi^n$.

The accuracy of the pusher is tested in appendix A in an axisymmetric, stationary JOREK equilibrium through conservation of energy and canonical toroidal momentum P_ϕ, showing the expected second-order scaling of the Boris method, and leading to a timestep requirement of 10^{-8} s or smaller for acceptable accuracy. We choose a timestep of 10^{-9} for extra safety margin.

After each particle position update, the new JOREK element-local coordinates need to be calculated, since the iso-parametric finite element discretisation in JOREK[12], mapping the element-local coordinates $\xi = (s, t, i_{\mathrm{elm}})$ to real-space coordinates $\mathbf{x} = (R, Z)$ is not analytically invertible. We can calculate the new element-local coordinates ξ by using Newton's method to solve $\mathbf{x} = F(\xi)$. Since space in the elements is typically only weakly distorted, this converges in only a few iterations. We use a tolerance here of 10^{-12} m in the L_2-norm. Particles that leave the domain are assumed to be lost.

To speed up the search when no nearby position is known, e.g. in the beginning of the simulation, we implement an R-Tree[20] which indicates the possible elements containing a point $\mathbf{x}$. Then we use several starting points in this element as initial guesses for the same algorithm described above.

An interpolation in time between the output files of JOREK is also required, which are generally not equidistant in time. For this we use third-order Hermite-Birkhoff interpolating functions, with the local derivatives estimated using non-uniform second order finite differences, a slight improvement on the method em-

ployed in[21]. This yields a C^1-continuous interpolation, which is important since the toroidal electric field is related to the time derivative of the poloidal magnetic flux ψ in the JOREK reduced MHD models[22].

Particle positions are initialised by a rejection sampling algorithm, which can take arbitrary functions of the MHD and space variables, but is used to sample uniformly in this work. Once the particle positions have been chosen, the velocity is sampled from the local Maxwellian velocity distribution and the charge is sampled from the coronal equilibrium charge state distribution. No other particle sources, like sputtering, are implemented, since any sputtered particles are very unlikely to make it into the core plasma during this simulation of a single ELM crash.

After each particle step the ionisation and recombination probabilities in that time are calculated from the ADAS ADF11 dataset, at the interpolated local electron temperature and density. Charge-exchange processes are not included. The particle charge is then updated by drawing two uniform random numbers u_i, u_r on $[0, 1]$ and ionizing or recombining if the probability is greater than u_i or u_r respectively.

This code improves upon earlier modelling of W transport in stationary fields (for instance IMPGYRO[23], SOLPS[24]) by having time-dependent electromagnetic fields. The plasma background evolution is not affected by impurity dynamics.

Particle-background collisions are not included in the present model as a first approximation, since the collisional slowdown time τ_s, seen in Table I, is comparable to the correlation time of the $E\times B$ drift velocity caused by the ELM (the ELM eddy turnover time of $\sim 100\mu$s) and the $E\times B$ drifts move every species in the plasma equally. This indicates that the influence of collisional processes on ELM-induced particle motion is limited. The particle-background collisions are however necessary for longer-time simulations, for instance to model impurity accumulation in the inter-ELM period, which we intend to address in future work.

Additionally it is important to note the length of the bounce time t_b and the

TABLE I. Typical values of W properties at the plasma core, top and bottom of the density pedestal. The temperature T, in keV, density in 10^{20} [m^{-3}], the safety factor q, the most probable charge state $q_{\rm mp}$, the sound speed $c_{s,W}$ in km/s, the gyrofrequency ω_g in MHz, the gyroradius r_g and the average banana orbit width w_b in mm, the average banana orbit period t_b in ms, the Coulomb logarithm $\ln\Lambda$ and the collisional slowdown time τ_s in ms, assuming a 0 and 1% concentration of beryllium in the plasma.

		ASDEX Upgrade[25,26]			JET[27]			ITER 15MA[28]		
		Core	Top	Bottom	Core	Top	Bottom	Core	Top	Bottom
T	[keV]	3	0.6	0.1	5	1.5	0.1	30	4.5	0.3
n_e	[10^{20} m^{-3}]	0.7	0.5	0.1	1.0	0.5	0.1	1.2	0.8	0.5
q	$=1/\iota$	1	5	6	1	3	6	1	3	6
$q_{\rm mp}$	[e]	42	24	14	47	30	14	65	45	19
$c_{s,W}$	[km/s]	69	31	13	88	48	13	220	80	20
ω_g	[MHz]	8	4	2	8	4	2	27	15	6
r_g	[mm]	1.1	1.0	0.7	1.5	1.5	0.9	1	0.7	0.4
w_b	[mm]	40	50	40	60	40	50	10	20	20
t_b	[ms]	2	4	10	3	2	2	0.5	3	19
$\ln\Lambda$		15	13	12	15	14	12	17	15	12
τ_s	[ms]	0.17	0.07	0.09	0.20	0.16	0.07	1.1	0.2	0.04
τ_s	[ms] (1% Be)	0.13	0.05	0.07	0.16	0.13	0.05	0.9	0.15	0.03

slow sound speed, noted in Table I for several devices. This means that W ions do not make many toroidal turns during an ELM crash, since their parallel velocity is low. This limits the contribution of radial W transport due to parallel motion along ergodic fieldlines, which will be further detailed in the next section.

III. W TRANSPORT IN AN ASDEX UPGRADE ELM

We follow W impurity particles initialized uniformly throughout the volume in a JOREK simulation of a convective type I ASDEX Upgrade ELM (#33616)[13,26], with parameters as in Table I. The simulated ELM-induced density losses are 7% and the duration is 2 ms, in good agreement with experimental results, indicating that $E\times B$ convective losses, causing the density losses, are reproduced realistically in the ELM simulation. The initial unstable mode is an $n=6$ peeling-ballooning mode, which later couples to $n=5$ and other toroidal mode numbers, in bursts

with an approximate period 0.2 ms and duration of 0.1 ms. The $n = 3 - 5$ modes are dominant, with $n > 6$ remaining strongly subdominant in this simulation, which includes diamagnetic flows. The energy losses are 2.5%.

Non-linear MHD simulations of ELMs at the low, experimental, values of the resistivity are challenging due to the small scale lengths in the current density at low resistivity. In this case, the resistivity is almost exactly matching the Spitzer resistivity with neoclassical corrections, differing by only a factor 4.[1] This can be considered the state of the art of what is presently possible in non-linear MHD simulations of ELMs. In this regime of low resistivity a further decrease by the factor of 4 is not likely to have a significant influence on the global size of the vortices and the $E \times B$ flow velocities.

To start the particle simulation, a total number of 10 million particles are sampled from a Maxwellian velocity distribution at the local background plasma temperature, with charge states determined from the coronal equilibrium distribution.

We then trace the paths of these particles in the nonlinear fields of the ELM simulation with a timestep of 10^{-9} s, which has been chosen after a convergence study shown (Appendix A). The particles make large radial excursions inwards and outwards during the ELM crash. In Figure 2 we show characteristic paths of particles that started with $\psi_n \in [0.895, 0.905]$. ψ_n is the poloidal magnetic flux, normalized to be 0 at the magnetic axis and 1 at the separatrix.

To investigate the motion of particles in the whole plasma due to the ELM we group all particles into a set of rings in ψ_n. The number density of particles from a specific ring is reconstructed using a Gaussian kernel density estimator on the number of particles with a specific ψ_n and dividing by the flux surface volume differential $\frac{dV}{d\psi_n}$. This reconstruction is shown at every 0.5 ms during the ELM in Figure 3. They show the spread in location of particles that started

[1] In the original publication[13] a factor of 8 was mentioned, since neoclassical corrections were not taken into account there.

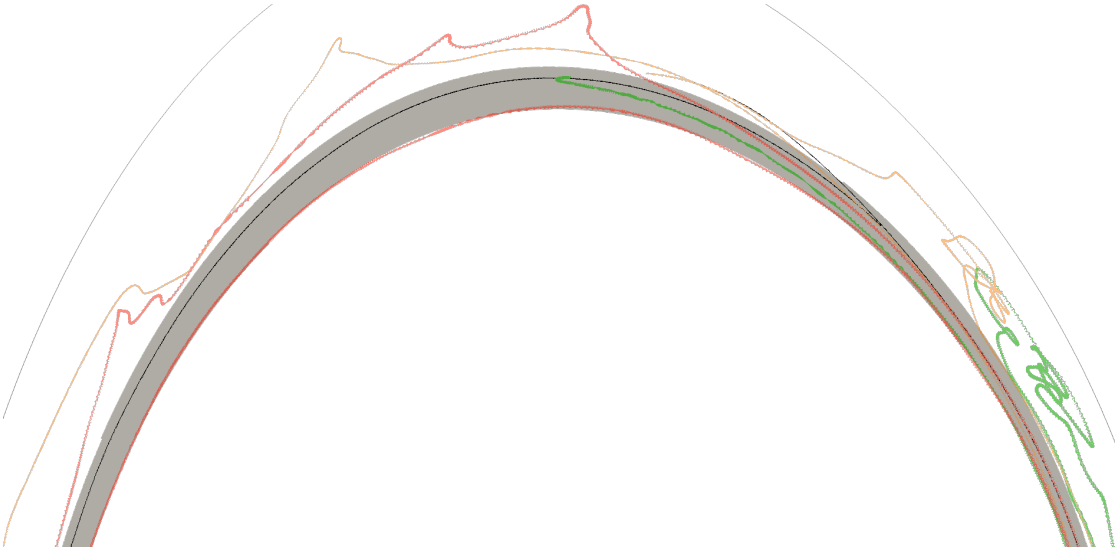

FIG. 2. Projection onto the poloidal plane of the paths of characteristic particles starting with $\psi_n \in [0.895, 0.905]$ (region shaded in grey). Different behaviours are observed, such as trapping and fast radial motion. The outer thin grey line is the separatrix. Particle paths are coloured for clarity.

in a specific interval in ψ_n. Particles that originated near the top of the density pedestal can be found inside up to $\psi_n = 0.75$, and outside the separatrix. Particles outside of the separatrix have moved inwards or have been lost to the wall and divertor. Transport to and from the private region (not shown in the figure) is small, in agreement with experimental observations that show ELM transport being outwards in the SOL.

There are two candidate mechanisms for radial transport, the $E \times B$-drift and the parallel transport of W along an ergodic magnetic field, which has small radial excursions leading to radial transport. We can distinguish between these by disabling the effect on the particles of either the non-axisymmetric electric or magnetic field component, which is caused by the peeling-ballooning mode. To test this we plot in Figure 4 the distribution of a single ring of particles over time with and without electric field perturbation, and with and without magnetic field perturbation. Disabling the non-axisymmetric component of the magnetic-field

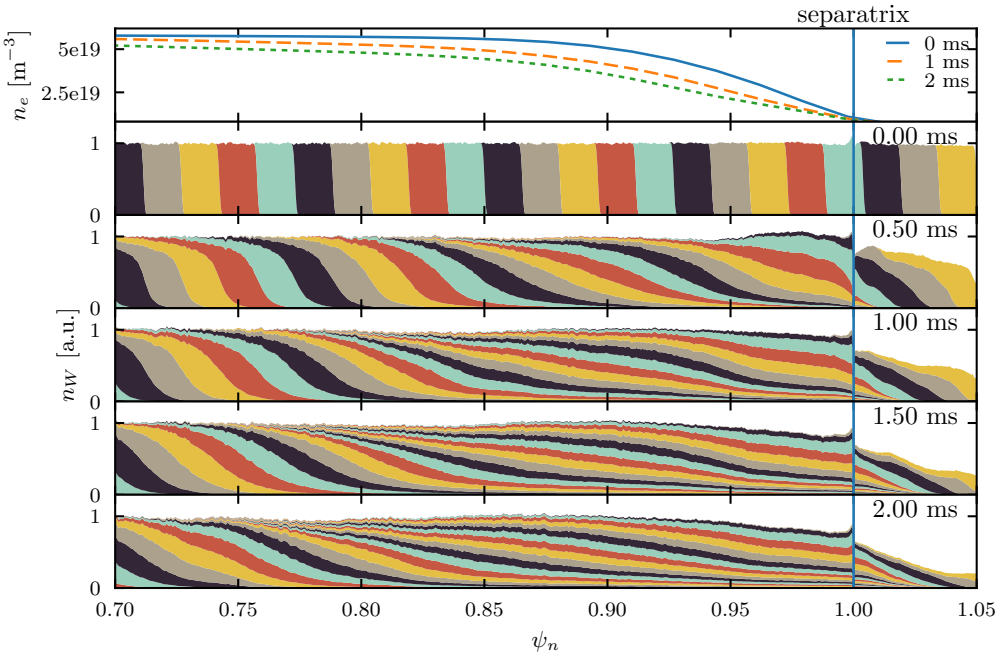

FIG. 3. Spreading of particles grouped in rings due to an ELM. The inward radial penetration of an ELM can be seen to increase during the whole ELM crash up to $t = 2$ ms. The top row contains the flux-surface averaged electron density every 1 ms after the onset of the ELM. The next rows contain the evolution of various tungsten density rings every 0.5 ms.

perturbation leads to no significant changes in the W density distribution. In all cases where the non-axisymmetric component of the electric field is zero no significant radial transport is visible. The electric field is thus a necessary ingredient for radial particle motion, which indicates the $E\times B$-drift as the cause. The $E\times B$-drift is parallel to the isolines of the potential perturbation in the poloidal plane to first order in $|\nabla\psi|/|F_0|$, drawn in figure 5. The radial $E\times B$-drift velocity is shown in Figure 6 at 0.5-ms intervals after the start of the ELM. The figure shows the $E\times B$-drift velocity distribution be time-varying and present far into the core plasma, with radial velocities of up to 5000 s^{-1}, which indicates a drift of one minor radius in 0.2 ms. There is no preferential radial direction, i.e. the

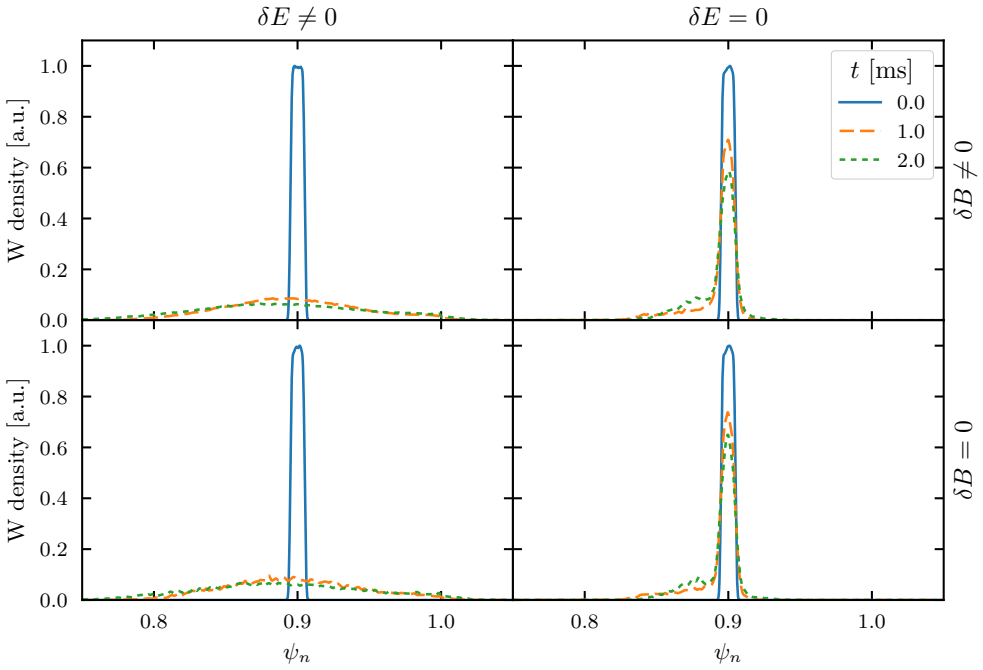

FIG. 4. Redistribution of a set of particles starting at $\psi_n \in [0.87, 0.88]$, shown at $t = 0, 1, 2$ ms. The top row has no magnetic perturbations, the right column has no non-axisymmetric electric field. The groups are reconstructed through Gaussian kernel density estimation with a smoothing factor of 0.002. The difference between rows indicates that the electric field perturbation is necessary for the redistribution, whereas the rows are similar, indicating the limited effect of the magnetic field perturbations.

distributions are symmetric around the point of zero radial motion.

We compare the W particle radial motion with the $E\times B$-drift velocity in Figure 7, for particles just inside the top of the pedestal, during a short period around $t = 1.025$ ms. It shows a Gaussian core with longer tails, with approximately exponential decay. The distribution is also almost symmetric, with a mean value of -1.6 s^{-1} meaning that as many trajectories move inwards as outwards at this point. The measured distribution is in close agreement with the radial $E\times B$-drift velocities in s^{-1}:

$$v_{\psi_n} = \frac{\mathbf{E} \times \mathbf{B}}{|B|^2} \cdot \nabla \psi_n. \tag{9}$$

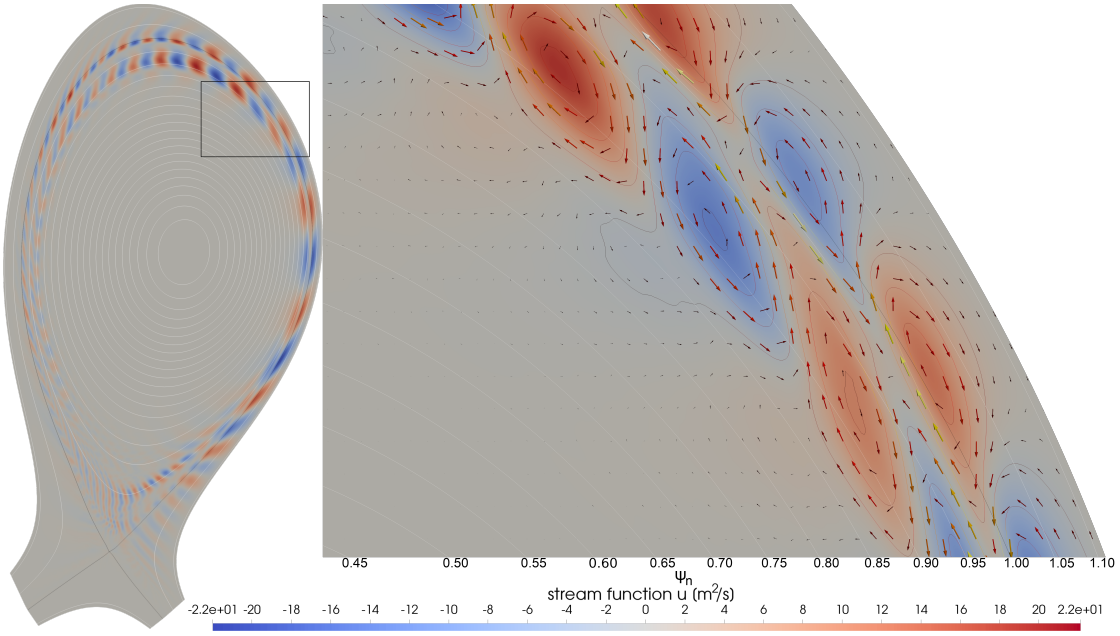

FIG. 5. The velocity stream function u of the ELM fields (left) with an inset including also $E\times B$ drift of particles in an ELM at $t = 0.3$ ms. Arrows indicate the direction of the drift, with the color indicating the magnitude $|v|$ and $\sqrt{|v|}$ as the length. The velocity stream function isolines are colored with the local velocity magnitude $|v|$. Labels below the inset indicate the value of ψ_n.

The motion of W particles due to the ELM can thus be characterized as a localized interchange motion, with roughly similar proportions of particles moving radially inwards and outwards. This will act to flatten any steep density gradients.

To look at time-resolved motion, we compare the kinetic energy of the MHD perturbation against v_r and v_r^2, the first and second moment of the particle velocity distribution at each radial location in Figure 8 during 2 ms after the ELM onset. These are calculated as

$$v_r(\psi_n, t) = \frac{1}{N\Delta t}\sum_{j=1}^{N}\left(\psi_n^{i+1} - \psi_n^i\right)_j \tag{10}$$

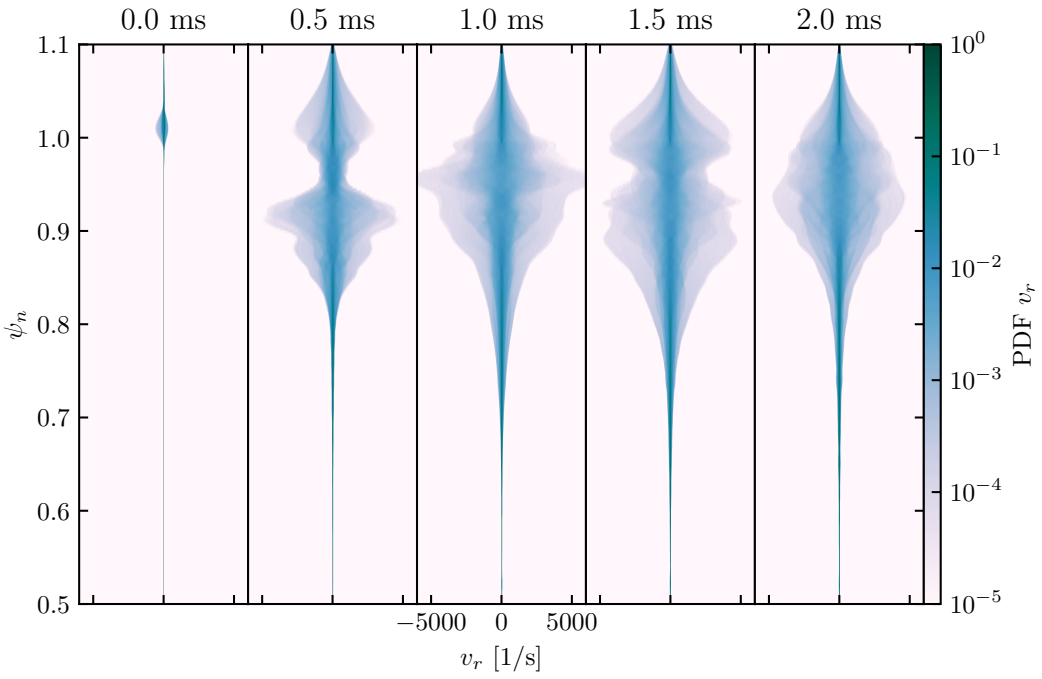

FIG. 6. Radial $E\times B$-drift velocity distribution function v_r for radial locations $\psi_n \in [0.5, 1.1]$, normalized per flux-surface and colored in log-scale, at 0, 0.5, 1.0, 1.5 and 5 ms after the start of the ELM.

and

$$v_r^2(\psi_n, t) = \frac{1}{N\Delta t^2} \sum_{j=1}^{N} \left(\psi_n^{i+1} - v_r(\psi_n^i, t)\Delta t - \psi_n^i\right)_j^2, \tag{11}$$

where j numbers the radial bins and i numbers the snapshots, at time-increments of Δt. There is a clear correlation between the peaks in kinetic mode energy E_{kin} and v_r^2, which characterizes the strength of the interchange motion. This shows that the radial transport is intermittent on the timescale of the eddy turnover time $\tau = 0.18$ ms.

To find the effect of this ELM on a specific W density distribution we weigh the uniformly distributed particles with three initial profiles and calculate the time-evolution. The first is a W impurity profile which resembles that of the electron density in H-modes, shown in Figure 9. We show that the ELM causes a net

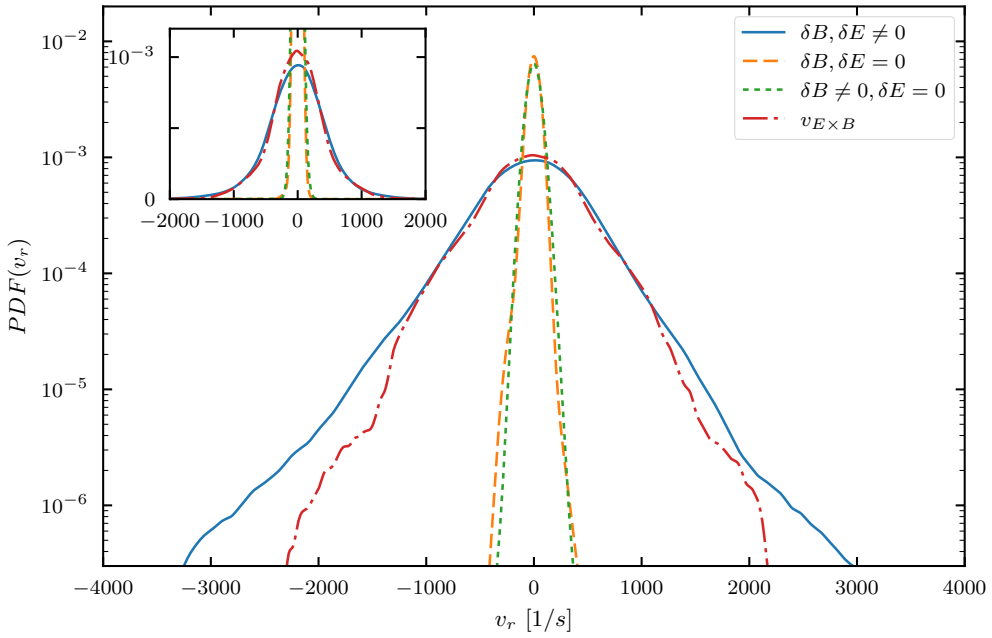

FIG. 7. Radial velocity distribution of particles with $\psi_n(t_0) \in [0.94, 0.96]$, integrated over $t = 1.0 - 1.05$ ms, and radial $E\times B$-velocity in the same ψ_n at t=1.025 ms. The inset shows the same plot on a linear scale. The radial drift velocities found agree very well with the $E\times B$-drift velocities.

movement of particles into the SOL coming from the region $\psi_n \in [0.75, 0.95]$. The density that establishes there is roughly half the initial density inside the pedestal. At $\psi_n = 0.85 - 0.9$,the density does not change much after the first millisecond, while further inside the plasma, particles are still moved outwards.

The second W profile, in Figure 10, has a maximum near the pedestal top. This has been observed in experiments when the density and temperature pedestals are not aligned[29]. This local W pedestal peak disappears completely during the ELM. Most of the particles in the peek region are moved outside of the pedestal. This corresponds well to results in earlier modelling of edge transport of W[30]. Besides this, the behaviour is similar to that shown in Figure 9.

Finally, in Figure 11 we look at a distribution where W is strongly screened,

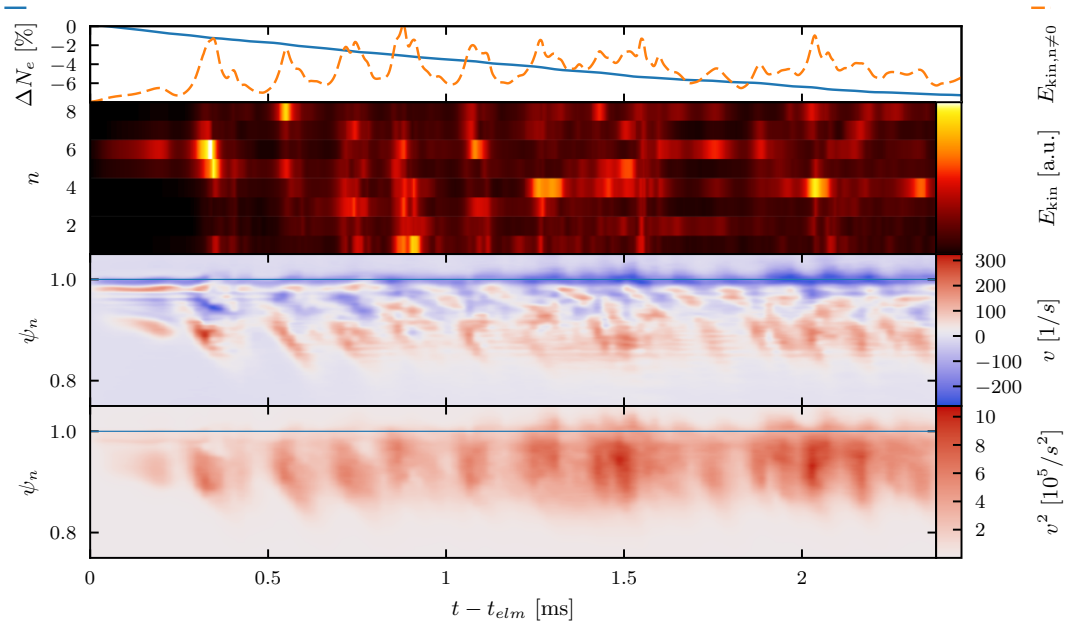

FIG. 8. Top pane shows the plasma density loss over time (blue) and the kinetic energy of the MHD perturbation (orange). Below that, the kinetic energies in different toroidal harmonics with dominant mode numbers n=1-6 in agreement with experimental observations[26]. The lower middle pane shows the mean radial velocity, and the bottom pane shows the mean square of radial velocity, both averaged over $\Delta t = 2 \cdot 10^{-5}$ s.

leading to W profiles which are hollow in the pedestal region. In this case, we obtain large particle losses to the divertor and wall, and inward penetration of 10-20% of W. From our results, it becomes clear that W expulsion by ELMs, when there is good W screening in the pedestal, will be very ineffective as also identified with a diffusive ELM model[7,31], and a few 10 % of the W outside the pedestal can actually be transported inside it in some cases by the ELM crashes.

IV. COMPARISON WITH 1D DIFFUSIVE MODELS

Simple 1D diffusive models are commonly used to estimate the effect of ELMs on impurity distributions, such as in[6,30]. The peeling-ballooning mode vortices lead to an interchange-type mode which is however not properly described in 1D

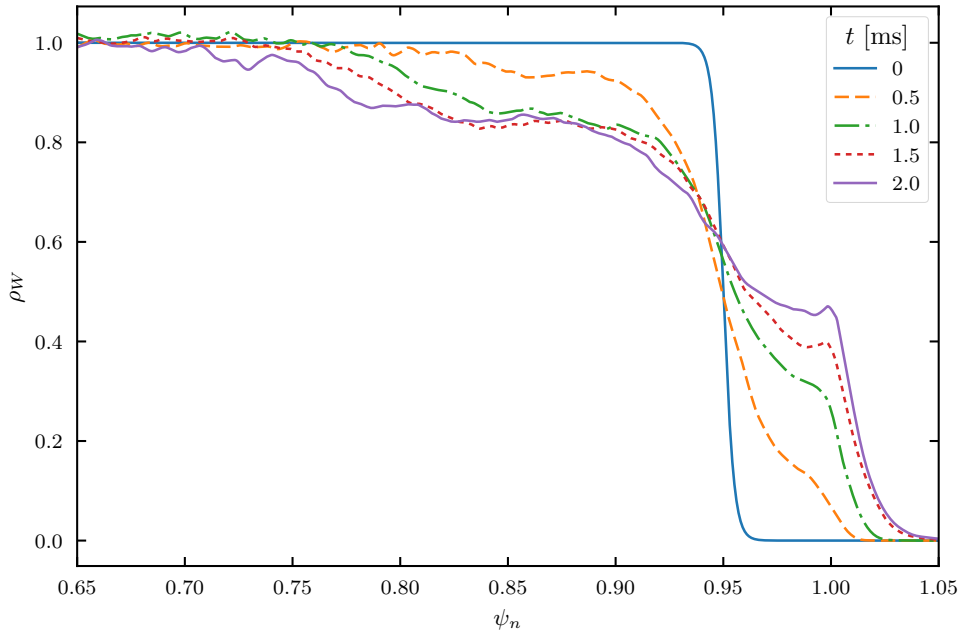

FIG. 9. A W impurity distribution with a profile similar to that of the electron density before an ELM, and at 0.5 ms intervals.

by a diffusive model, since the trajectory of the particle depends on the mode phase and not just on the radial position. The strength of the $E\times B$-drift varies locally with the mode amplitude, on a length scale comparable to the radial excursions of the particle, i.e. the ballistic length of transport is comparable to the system size. Additionally, the characteristic time scale of the particle radial velocity, the eddy turnover time $\tau = 0.18$ ms, indicates that, since diffusive-like behaviour can only be seen after many ballistic times, a diffusion coefficient can only be defined on a time scale of multiple milliseconds. Nonetheless, it is relevant to compare the performance of diffusive models with the full trajectory calculations in this paper, to see how they perform.

We can make a rough estimate of a diffusion coefficient from the length scale and typical velocity, at for instance $t = 1.0 - 1.05$ ms at $\psi_n = 0.95$ by calculating the

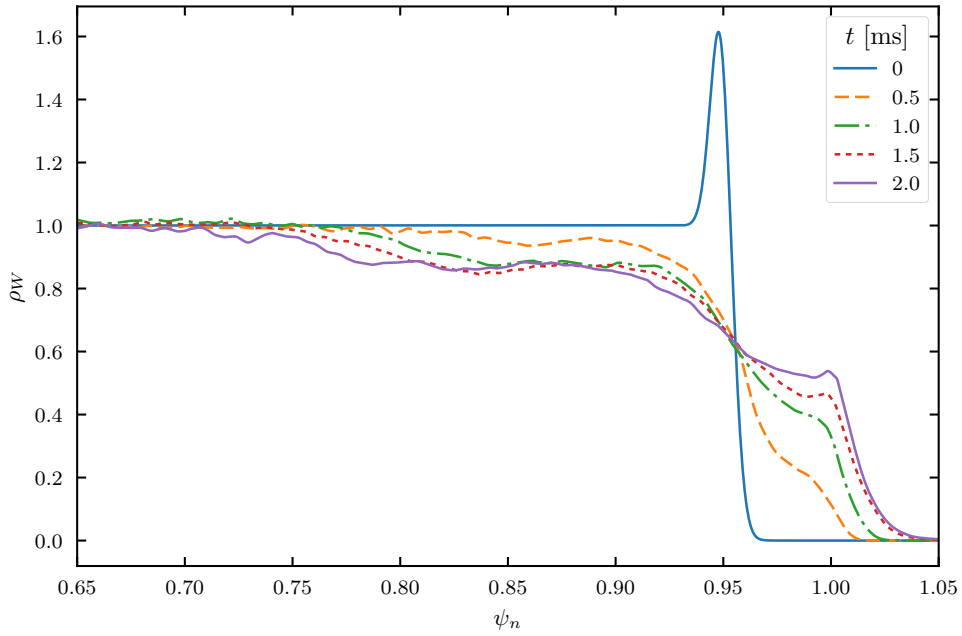

FIG. 10. Profile of a distribution with edge W density peaking, which can be caused due to neoclassical transport when the temperature and density pedestals are not coincident, at 0.5 ms intervals after ELM onset.

RMS of the radial velocity distribution in Figure 7, $\sqrt{\langle v_r^2 \rangle} = 497$ /s. Multiplying this with the approximate vortex radius (See Figure 5) $r_v = 0.015$ gives us

$$D_{\psi_n} \approx \sqrt{\langle v_r^2 \rangle} r_v = 7.5 \ /s. \tag{12}$$

To estimate the magnitude of the diffusion coefficient in m^2/s we can multiply this by the flux-surface average of $1/|\nabla\psi_n|^2$, which is (at $\psi_n = 0.95$) 1.51 m^2, corresponding to $D_r \approx 11$ m^2/s which is comparable to the diffusion coefficients used in literature[6,30], though, since only two rows of vortices are present the diffusive effects will be highly localized.

Additionally, from the microscopic trajectories, we can estimate a local diffusion coefficient. In a homogeneous medium and on timescales much longer than that

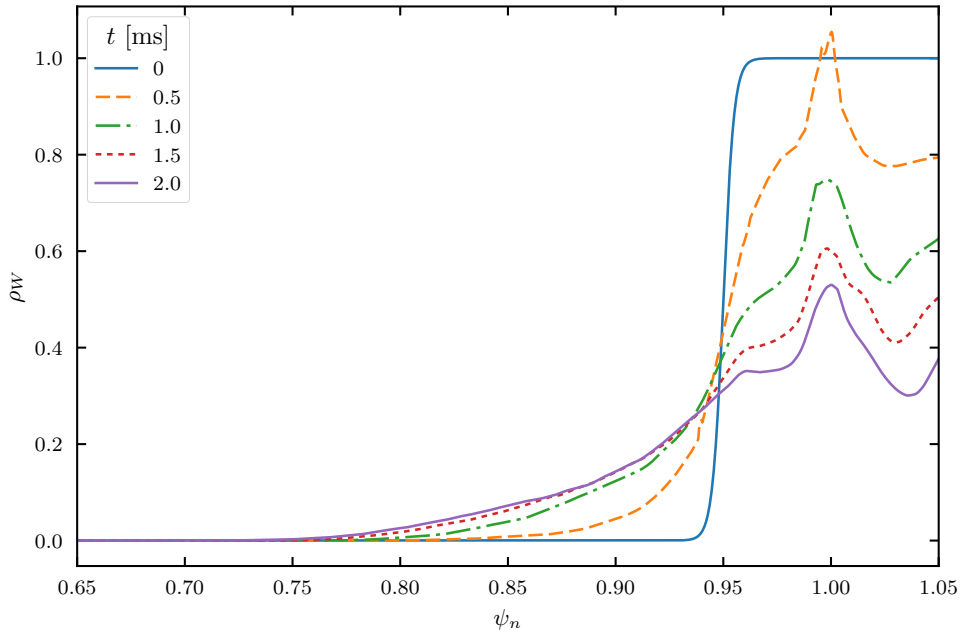

FIG. 11. Profile of a W density distribution with dominant screening in the pedestal at 0.5 ms intervals after ELM onset.

of the driving force, this can be measured from the mean-squared displacement

$$2D_{\psi_n} t = \left\langle (\psi_n(t) - \psi_n(0))^2 \right\rangle , \tag{13}$$

where ψ_n denotes the position of a specific particle and the brackets denote an average over all particles in a region. In this case it is complicated by the locality of the driving forces in space and time. The time of our measurement needs to be small enough for the particles not to encounter significantly different diffusion coefficients. This means that our integration time must be much smaller than the ELM burst period. In space, we have the locality requirement as $\sqrt{2D_{\psi_n} t} \ll 0.05$, which is approximately the radius of the ballooning mode structure of the ELM. A scan of analysis timesteps shows $t = 0.02$ ms to be a suitable period, with the

calculated D_{ψ_n} not changing significantly for larger timesteps.

We can then determine transport coefficients from the moments of the particle radial velocity distribution, shown in Figure 8. The effective radial velocity contains both the real radial velocity as well as the contribution due to the spatial gradient of the diffusion coefficient driven by the divergence of the flux proportional to ∇n,

$$\frac{\partial n}{\partial t} = D\nabla^2 n + (\nabla D - v_r) \cdot \nabla n - (\nabla v_r) n. \tag{14}$$

Where the radial velocity v_r is closely related to the average radial $E\times B$drift of -0.4 /s, which varies very little during the ELM, and thus negligible compared to the ∇D radial velocity. We can obtain an estimate of the diffusion coefficient D_{ψ_n} from the second moment of the position distribution function, as

$$D_{\psi_n}(\psi_n, t) = \frac{\Delta t}{2} v_r^2. \tag{15}$$

To perform one-dimensional modelling, we calculate a time average over the ELM of D_{ψ_n} to obtain a smooth 1D profile, localized between $\psi_n = 0.80$ and $\psi_n = 1.05$, as seen in Figure 12.

We follow the evolution with our 6D model, with the 1D coefficients derived above as well as with one-dimensional diffusion coefficients approximated from[30], shown in Figure 12. These have been chosen to reproduce experimental ELM flushing behaviour[30] in STRAHL. This has negligible v/D during the ELM, and for D a gaussian profile with height 20 m^2/s, center 2 cm inwards from the separatrix and $\sigma = 3.5$ cm, which we translate to ψ_n-coordinates[2] as

$$D_{\text{ref}} = 6.5 \cdot \exp\left(\frac{-(\psi_n - 0.98)^2}{2 \cdot 0.028^2}\right) \tag{16}$$

where we kept the diffusion coefficient constant over time (instead of linearly de-

[2] using the flux-surface average of $1/|\nabla\psi_n|^2$, which is (at $\psi_n = 0.95$) 1.51 m^2 as a length scale.

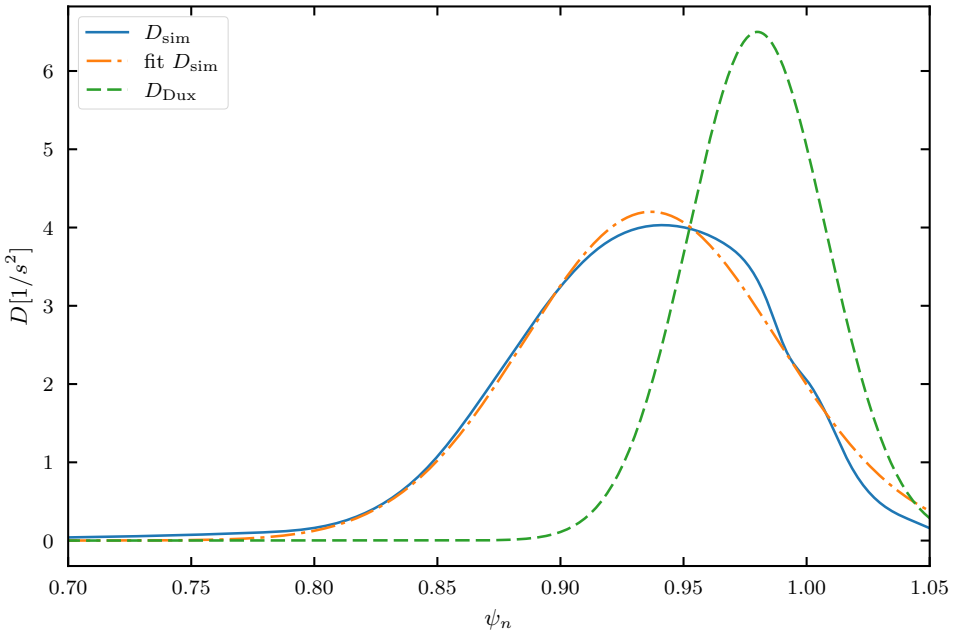

FIG. 12. The calculated diffusion coefficient, a fit with a Gaussian ($A = 4.2, \mu = 0.94, \sigma = 0.05$) and the diffusion coefficient used in[30].

creasing), since this corresponds better to the character of radial and interchange motions seen in Figure 8, but have decreased the strength by a factor of 2 to compensate. It is peaked slightly further outwards than our derivation from particle trajectories.

In the 1D modelling we include a sink in the SOL, modelled as in[30] with a parallel connection length $L_\parallel = 50$ m, a loss frequency

$$\nu_\parallel = \frac{2v_{\parallel,W}}{L_\parallel}, \tag{17}$$

an impurity velocity

$$v_{\parallel,W} \approx v_{\parallel,D} = M\sqrt{\frac{k_B(3T_i + T_e)}{m_D}} = 10\mathrm{km/s} \tag{18}$$

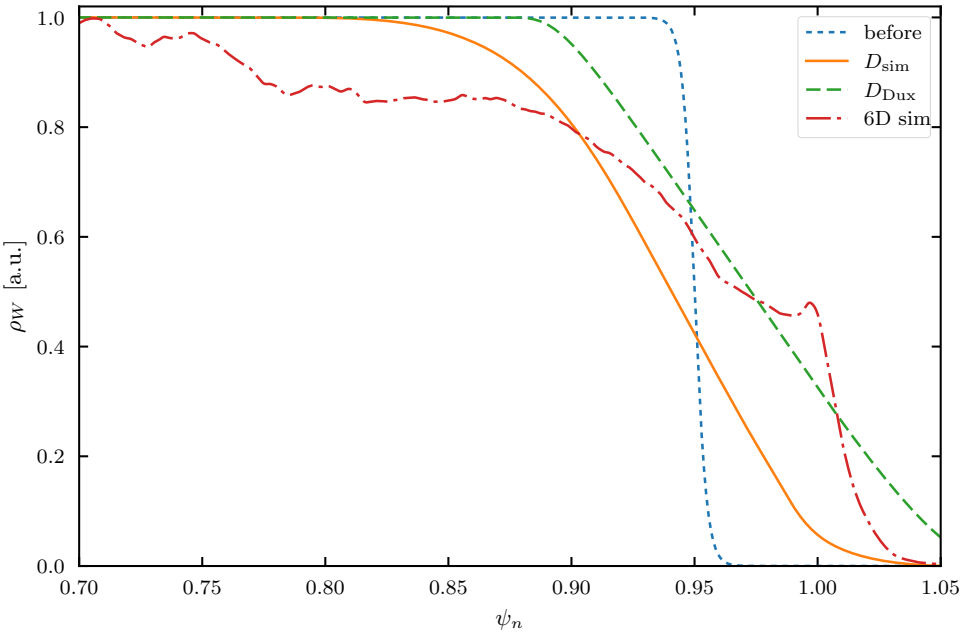

FIG. 13. A W impurity distribution with a profile similar to that of the electron density after an ELM, compared with two diffusive models. The diffusive models show the same qualitative behaviour, but cannot reproduce the steepness of the profiles after our simulation or the inwards extent of flushing.

at $T_i = T_e = 100$ eV, with a Mach number of 0.07. This leads to $\nu_{\parallel} = 387/$ s, corresponding well with the estimate we can make from the evolution of the impurity distribution in Figure 11, where 50% of the SOL density is removed in 2 milliseconds, leading to $\nu_{\parallel,\mathrm{est}} = \frac{-\ln(0.5)}{2\mathrm{ms}} = 346$ /s.

In the case where all impurities start inside the pedestal, i.e. Figure 13, the Dux diffusion coefficients overestimate flushing into the far SOL, but reasonably reproduce the total amount of flushing. The inwards extent of the impurity flushing is however not reproduced well by either of the models. Particles are drawn from much farther inside the plasma than the diffusive modelling suggests. In the related case, including edge peaking of the impurity distribution, the behaviour is similar 14.

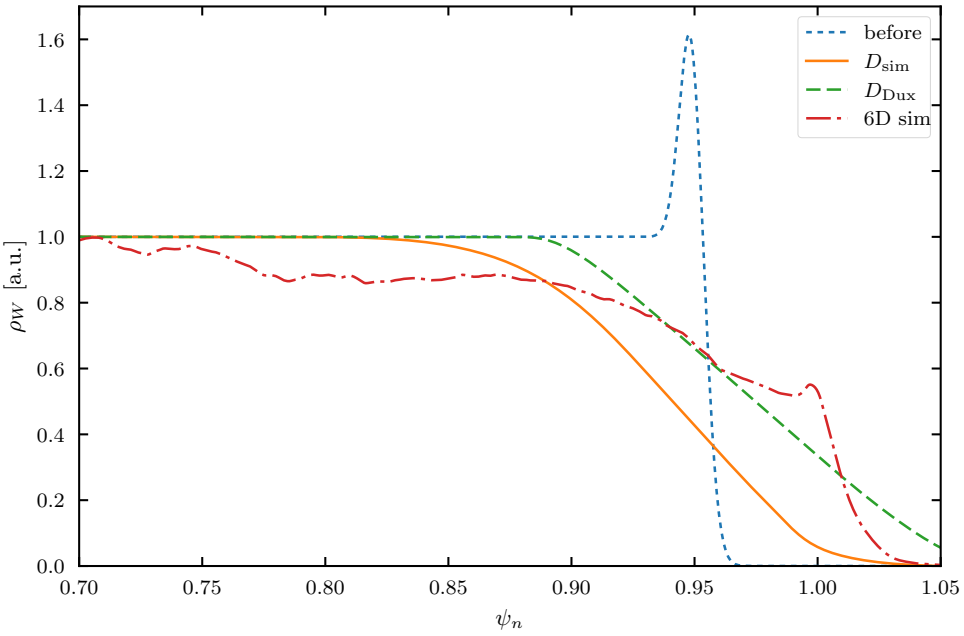

FIG. 14. Profile of a distribution with edge W density peaking after an ELM, compared with two diffusive models. Qualitatively the diffusive models show the same behaviour, though the flushing from inside the peak is not reproduced.

The inverted profile, where W is screened and the concentration outside of the pedestal is higher than inside, the Dux model and to a lesser extent the 1D model presented here, underestimate the inwards motion of W. The losses from the SOL are modelled well, as well as the general characteristics of the motion.

To first order the W transport from the 3D interchange motion of the ELM ballooning mode can be approximated by a 1D radial diffusion process, in the sense that any, positive or negative, gradient in the initial profiles will be reduced. The 1D radial diffusion process however does not describe well the after-ELM radial W profile as the W losses with the 1-D model do not reach as far inwards and outwards as those of the 6-D model, and features such as the limited flattening of the gradient at the outwards moved edge imply a low diffusive component. This

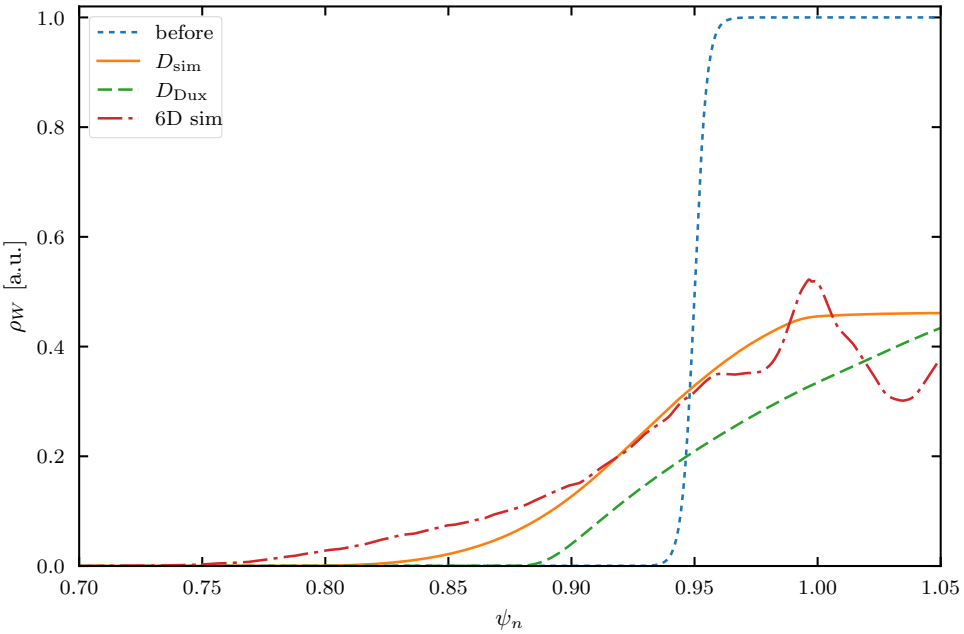

FIG. 15. Profile of a W density distribution with dominant screening in the pedestal after an ELM, compared with two diffusive models. The 6D model shows further inward penetration than the diffusive models, but there is good qualitative agreement.

is incompatible with the 1-D modelling results and illustrates the limitation of applying simple models to W particle expulsion by ELMs.

V. CONCLUSIONS

Our 6D simulation of W impurity transport in an ASDEX Upgrade ELM crash show very efficient transport in the pedestal region, with particles being redistributed in a region of $\psi_n \in [0.75, 1.05]$. W impurities from the top of the pedestal are expelled into the SOL while those near and just inside the separatrix are brought inwards by the ELM.

W transport is found to be due to the electric fields from the peeling-ballooning MHD instability causing an ELM. The transport due to magnetic field pertur-

bations is negligible. Effective radial transport, i.e. averaged over flux surfaces, is to first order diffusive, but this 1D description lacks many features of the W particle motion observed here, such as the inward extent of flushing of particles inside $\psi_n = 0.85$. This is to be expected in the case of a strong interchange motion, where a diffusive model is not a completely appropriate description.

The very large inward and outward W fluxes created by the ELM have particularly important consequences for W expulsion when W is well screened in the pedestal between ELMs. In this case, the 6-D model applied here indicates that the ELMs will actually cause an increase of the W density in the confined plasma rather than a reduction. The experimental validation of this finding is essential to assess the viability of ELMs as the mitigation approach to provide W exhaust in ITER scenarios.

Acknowledgements

The authors thank Priv.-Doz. Dr. T. Pütterich, Prof. Dr. N.J. Lopes Cardozo, Dr. D. Hu and Dr. T. Weyens for fruitful discussions and comments.

This work has been partly carried out within the framework of the EUROfusion Consortium and has received funding from the Euratom research and training programme 2014–2018 under grant agreement number 633053. The views and opinions expressed herein do not necessarily reflect those of the European Commission.

Simulations have been performed on the EUROfusion High Performance Computer (Marconi-Fusion).

ITER is the Nuclear Facility INB no. 174. The views and opinions expressed herein do not necessarily reflect those of the ITER Organization.

REFERENCES

[1]R. A. Pitts, S. Carpentier, F. Escourbiac, T. Hirai, V. Komarov, S. Lisgo, A. S. Kukushkin, A. Loarte, M. Merola, A. Sashala Naik, R. Mitteau, M. Sugihara, B. Bazylev, and P. C. Stangeby, "A full tungsten divertor for ITER: Physics issues and design status," J. Nucl. Mater. **438**, S48–S56 (2013).

[2]J. P. Gunn, S. Carpentier-Chouchana, R. Dejarnac, F. Escourbiac, T. Hirai, M. Komm, A. Kukushkin, S. Panayotis, and R. A. Pitts, "Ion orbit modelling of ELM heat loads on ITER divertor vertical targets," Nucl. Mater. Energy **12**, 75–83 (2017).

[3]R. Neu, R. Dux, A. Geier, O. Gruber, A. Kallenbach, K. Krieger, H. Maier, R. Pugno, V. Rohde, and S. Schweizer, "Tungsten as plasma-facing material in ASDEX Upgrade," Fusion Eng. Des. **65**, 367–374 (2003).

[4]I. Nunes, "Plasma confinement at JET," Plasma Phys. Control. Fusion **58**, 014034 (2016).

[5]M. Wade, K. Burrell, A. Leonard, T. Osborne, and P. Snyder, "Edge-localized-mode-induced transport of impurity density, energy, and momentum," Phys. Rev. Lett. **94**, 1–4 (2005).

[6]T. Pütterich, R. Dux, M. A. Janzer, and R. M. McDermott, "ELM flushing and impurity transport in the H-mode edge barrier in ASDEX Upgrade," J. Nucl. Mater. **415**, 334–339 (2011).

[7]R. Dux, A. Loarte, E. Fable, and A. Kukushkin, "Transport of tungsten in the H-mode edge transport barrier of ITER," Plasma Phys. Control. Fusion **56**, 124003 (2014).

[8]E. R. Solano, E. A. Autricque, I. Coffey, E. Delabie, E. D. Luna, P. Drewelow, L. Frassinetti, M. Clever, I. Nunes, T. Loarer, A. Meigs, F. Rimini, and M. Stamp, "Effect of fuelling location on pedestal and ELMs in JET," in *41st EPS Conf. Plasma Phys.* (2014).

[9]N. Den Harder, S. Brezinsek, T. Pütterich, N. Fedorczak, G. Matthews, A. Meigs,

M. Stamp, M. van de Sanden, and G. Van Rooij, "ELM-resolved divertor erosion in the JET ITER-Like Wall," Nucl. Fusion **56**, 026014 (2016).

[10]R. Dux, A. Loarte, C. Angioni, D. Coster, E. Fable, and A. Kallenbach, "The interplay of controlling the power exhaust and the tungsten content in ITER," Nucl. Mater. Energy **0**, 1–8 (2016).

[11]G. Huysmans and O. Czarny, "MHD stability in X-point geometry: simulation of ELMs," Nucl. Fusion **47**, 659–666 (2007).

[12]O. Czarny and G. Huysmans, "Bézier surfaces and finite elements for MHD simulations," J. Comput. Phys. **227**, 7423–7445 (2008).

[13]M. Hoelzl, G. T. Huijsmans, F. Orain, F. J. Artola, S. Pamela, M. Becoulet, D. van Vugt, F. Liu, S. Futatani, A. Lessig, E. Wolfrum, F. Mink, E. Trier, M. Dunne, E. Viezzer, T. Eich, B. Vanovac, L. Frassinetti, S. Guenter, K. Lackner, and I. Krebs, "Insights into type-I edge localized modes and edge localized mode control from JOREK non-linear magneto-hydrodynamic simulations," Contrib. to Plasma Phys. , 1–11 (2018).

[14]F. J. Artola, G. T. Huijsmans, M. Hoelzl, P. Beyer, A. Loarte, and Y. Gribov, "Non-linear magnetohydrodynamic simulations of edge localised mode triggering via vertical position oscillations in ITER," Nucl. Fusion **58** (2018), 10.1088/1741-4326/aace0e.

[15]D. C. van Vugt, G. T. A. Huijsmans, M. Hoelzl, S. Q. Korving, S. Franssen, D. Hu, S. Pamela, A. Dvornova, C. Sommariva, A. Loarte, and N. J. Lopes Cardozo, "Coupled nonlinear MHD-particle simulations in JOREK," in preparation.

[16]J. P. Boris, "Relativistic plasma simulation-optimization of a hybrid code," in *Proc. Fourth Conf. Num. Sim. Plasmas* (1970) pp. 3–67.

[17]C. K. Birdsall and A. B. Langdon, *Plasma Physics via Computer Simulation*, Series in Plasma Physics (Taylor & Francis, 2004).

[18]O. Buneman, "Time-reversible difference procedures," J. Comput. Phys. **1**, 517–

535 (1967).

[19]G. L. Delzanno and E. Camporeale, "On particle movers in cylindrical geometry for Particle-In-Cell simulations," J. Comput. Phys. **253**, 259–277 (2013).

[20]A. Guttman, "R-trees," Proc. 1984 ACM SIGMOD Int. Conf. Manag. data - SIGMOD '84 , 47 (1984).

[21]C. Sommariva, E. Nardon, M. Hoelzl, G. Huijsmans, and D. van Vugt, "Simulation of relativistic test electron transport in a JET disruption," Nucl. Fusion , 17–22.

[22]F. Orain, M. Bécoulet, G. Dif-Pradalier, G. Huijsmans, S. Pamela, E. Nardon, C. Passeron, G. Latu, V. Grandgirard, A. Fil, A. Ratnani, I. Chapman, A. Kirk, A. Thornton, M. Hoelzl, and P. Cahyna, "Non-linear magnetohydrodynamic modeling of plasma response to resonant magnetic perturbations," Phys. Plasmas **20**, 102510 (2013).

[23]S. Yamoto, X. Bonnin, Y. Homma, H. Inoue, K. Hoshino, A. Hatayama, and R. A. Pitts, "Kinetic modeling of high-Z tungsten impurity transport in ITER plasmas using the IMPGYRO code in the trace impurity limit," Nucl. Fusion **57** (2017), 10.1088/1741-4326/aa7fa6.

[24]X. Bonnin and D. Coster, "Full-tungsten plasma edge simulations with SOLPS," J. Nucl. Mater. **415**, S488–S491 (2011).

[25]B. Vanovac, E. Wolfrum, S. S. Denk, F. Mink, F. M. Laggner, G. Birkenmeier, M. Willensdorfer, E. Viezzer, M. Hoelzl, S. J. Freethy, M. G. Dunne, A. Lessig, and N. C. Luhmann, "Effects of density gradients and fluctuations at the plasma edge on ECEI measurements at ASDEX Upgrade," Plasma Phys. Control. Fusion **60** (2018), 10.1088/1361-6587/aaa7ac.

[26]A. Mink, M. Hoelzl, E. Wolfrum, F. Orain, M. Dunne, A. Lessig, S. Pamela, P. Manz, M. Maraschek, G. Huijsmans, M. Becoulet, F. Laggner, M. Cavedon, K. Lackner, S. Günter, and U. Stroth, "Nonlinear coupling induced toroidal structure of edge localized modes," Nucl. Fusion **58**, 026011 (2018).

[27]G. T. A. Huijsmans, F. Liu, S. Futatani, A. Loarte, F. Köchl, M. Hoelzl, A. M. Garofalo, and E. Nardon, "Non-Linear MHD simulations for ITER," in *Proc. 25th IAEA Fusion Energy Conf. St. Petersburg, Russ.* (2014) pp. Th/6–1Ra.

[28]C. E. Kessel, D. Campbell, Y. Gribov, G. Saibene, G. Ambrosino, T. Casper, M. Cavinato, H. Fujieda, R. Hawryluk, L. D. Horton, A. Kavin, F. Koechl, J. Leuer, A. Loarte, P. J. Lomas, T. Luce, M. Mattei, I. Nunes, V. Parail, A. Polevoi, A. Portone, and R. Sartori, "Development of the ITER 15 MA ELMy H-mode Inductive Scenario," Nucl. Fusion **49** (2009).

[29]F. Koechl, A. Loarte, E. de la Luna, V. Parail, G. Corrigan, D. Harting, I. Nunes, C. Reux, F. Rimini, A. Polevoi, M. Romanelli, and JET Contributors, "W transport and accumulation control in the termination phase of JET H-mode discharges and implications for ITER," Plasma Phys. Control. Fusion , 1–8.

[30]R. Dux, A. Janzer, and T. Pütterich, "Main chamber sources and edge transport of tungsten in H-mode plasmas at ASDEX Upgrade," Nucl. Fusion **51**, 053002 (2011).

[31]A. R. Polevoi, A. Loarte, R. Dux, T. Eich, and E. Fable, "Integrated Simulations of H-mode Operation in ITER including Core Fuelling , Divertor Detachment and ELM Control," in *26th IAEA Fusion Energy Conf. (FEC 2016)* (2017) pp. 1–8.

Appendix A: Verification of the particle pusher

To prove the correctness of the particle pusher we check the conservation of kinetic energy K and of canonical toroidal momentum P_ϕ in an axisymmetric JOREK equilibrium without electric fields. This equilibrium is obtained by removing the electric field from the pre-ELM equilibrium described in Section III. W ions are initialized near the axis, with $\psi_N \in [0, 0.214]$ and with the velocities sampled from the local Maxwellian and charge state $Z = 10$. 10000 particles are

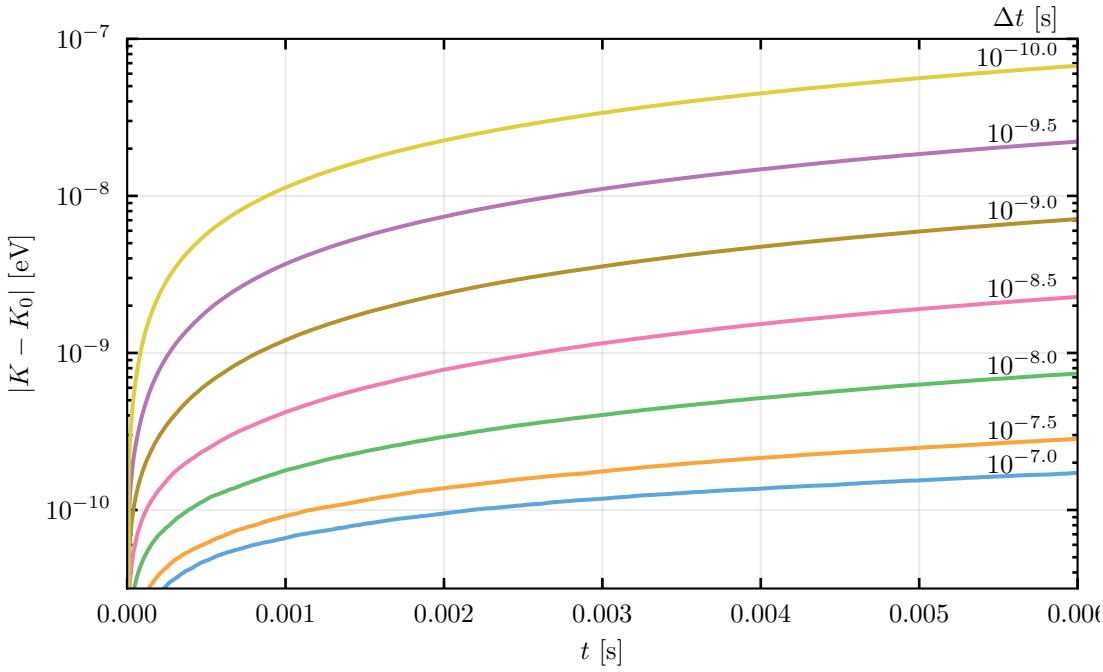

FIG. 16. Mean and maximum change in kinetic energy in eV.

followed for each of the timestep sizes tested, between 0.1 microsecond and 0.1 nanosecond.

Figure 16 shows the mean change in kinetic energy $< |K - K_0| >$ after the start of the simulation in eV. The error made here is negligible compared to the average value of the kinetic energy of ~ 4.1 keV. They grow as $\sqrt{t}$, indicating a random walk of floating-point roundoff errors per step. This also explains why the error increases with number of steps and hence decreases with timestep size.

Figure 17 shows the mean relative change in $P_\phi = Ze\psi - mRv_\phi$, a constant of motion. This is nearly constant throughout the simulation, showing that the particle trajectory integration is correct. A small drift is present at the smallest timestep sizes, but is far too small to play a role in our application. Decreasing the timestep size causes the conservation of P_ϕ to quadratically improve, as expected from the second-order Boris method. This is better illustrated in figure 18, where the solid line indicates the mean relative change and the violins show the

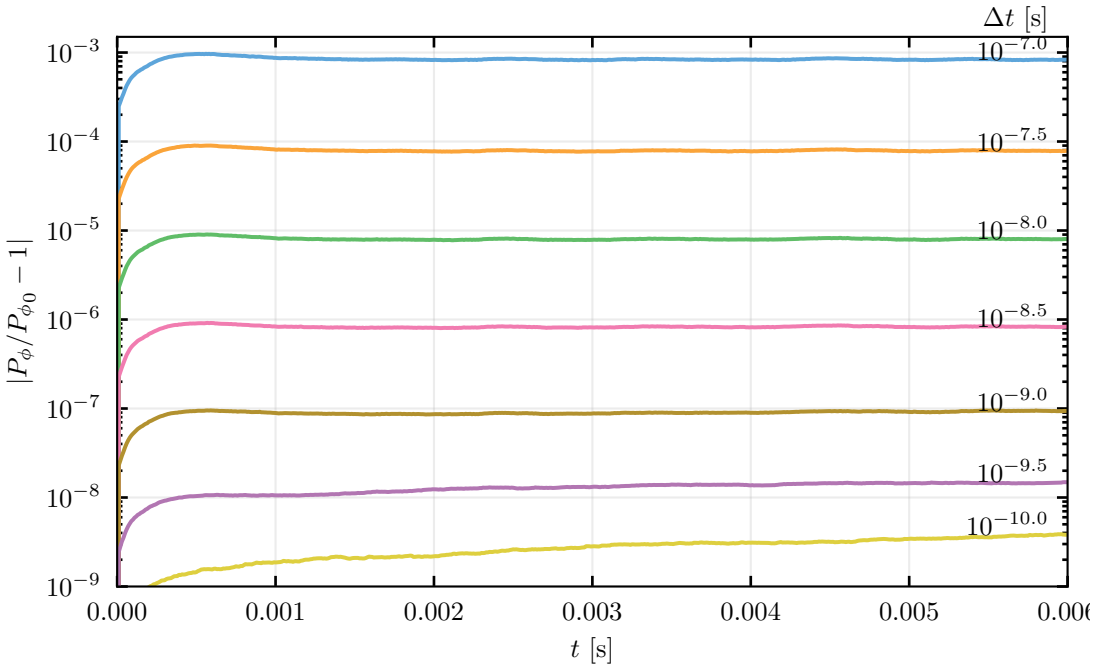

FIG. 17. Mean relative change in P_ϕ over time at different timestep sizes.

distribution of changes in P_ϕ. From this we can estimate a timestep size at which to run our simulations. Time steps smaller than 10^{-8} second seem adequate, since they lead to an acceptable mean relative variation of $8 \cdot 10^{-6}$ over 6 milliseconds of simulation time.

Appendix B: Convergence study of results with number of particles.

Figure 19 shows the scaling of reconstruction of tungsten profiles after an ELM with the number of particles. This shows that enough particles have been used to remove statistical variation. Particles followed have been placed pseudo-randomly in the plasma, leading to the scaling of $1/\sqrt{N}$ in the reconstruction.

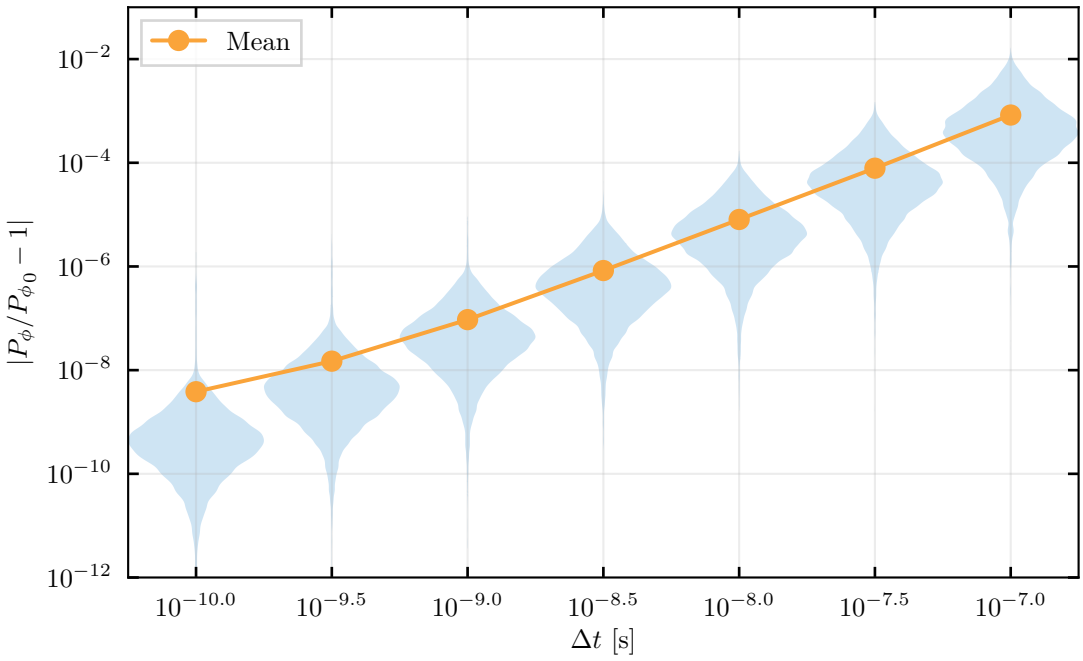

FIG. 18. Mean relative change in P_ϕ and distribution for different timestep sizes.

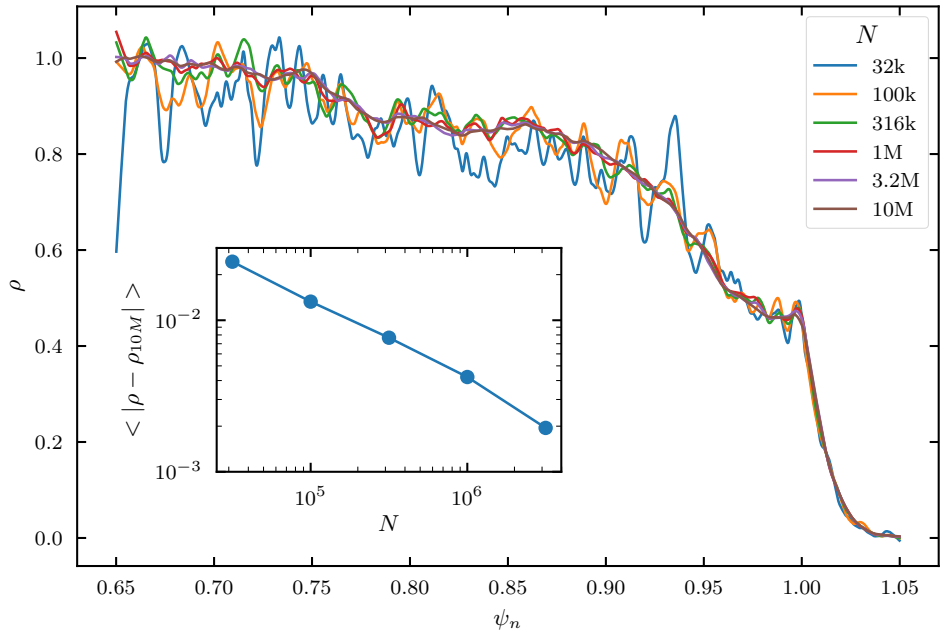

FIG. 19. Reconstruction of the electron H-mode pedestal-like W density profile after 2 ms with varying number of particles N. Inset shows the scaling of the mean absolute deviation to the results with 10 million particles, which has the expected $1/\sqrt{N}$-scaling for Monte-Carlo methods.